Angular dependence of photoemission time delay in helium

Sebastian Heuser[1], Álvaro Jiménez Galán[2], Claudio Cirelli[1*], Carlos Marante[2], Mazyar Sabbar[1], Robert Boge[1], Matteo Lucchini[1], Lukas Gallmann[1,3], Igor Ivanov[4,5], Anatoli S. Kheifets[4], J. Marcus Dahlström[6,7,8], Eva Lindroth[6], Luca Argenti[2], Fernando Martín[2,9,10], Ursula Keller[1]

[1]*Physics Department, ETH Zurich, 8093 Zurich, Switzerland*
[2]*Departamento de Química, Módulo 13, Universidad Autónoma de Madrid, 28049 Madrid, Spain*
[3]*Institute of Applied Physics, University of Bern, 3012 Bern, Switzerland*
[4]*Research School of Physics and Engineering, The Australian National University, Canberra ACT 0200, Australia*
[5]*Center for Relativistic Laser Science, Institute for Basic Science (IBS), Gwangju 500-712, Republic of Korea*
[6]*Department of Physics, Stockholm University, AlbaNova University Center, SE-10691 Stockholm, Sweden*
[7]*Max Planck Institute for the Physics of Complex Systems, Noethnitzerstr. 38, 01187 Dresden, Germany*
[8]*Center for Free-Electron Laser Science, Luruper Chaussee 149, 22761 Hamburg, Germany*
[9]*Instituto Madrileño de Estudios Avanzados en Nanociencia (IMDEA-Nanociencia), Cantoblanco, 28049 Madrid, Spain*
[10]*Condensed Matter Physics Center (IFIMAC), Universidad Autónoma de Madrid, 28049 Madrid, Spain*

Corresponding author:

Claudio Cirelli
Physics Department, ETH Zurich
Auguste-Piccard-Hof 1
CH-8093 Zurich
Switzerland
phone: +41 44 633 6530
e-mail: cirelli@phys.ethz.ch

Abstract

Time delays of electrons emitted from an isotropic initial state with the absorption of a single photon and leaving behind an isotropic ion are angle-independent. Using an interferometric method involving XUV attosecond pulse trains and an IR probe field in combination with a detection scheme, which allows for full 3D momentum resolution, we show that measured time delays between electrons liberated from the $1s^2$ spherically symmetric ground state of helium depend on the emission direction of the electrons relative to the common linear polarization axis of the ionizing XUV light and the IR probing field. Such time delay anisotropy, for which we measure values as large as 60 attoseconds, is caused by the interplay between final quantum states with different symmetry and arises naturally whenever the photoionization process involves the exchange of more than one photon. With the support of accurate theoretical models, the angular dependence of the time delay is attributed to small phase differences that are induced in the laser-driven continuum transitions to the final states. Since most measurement techniques tracing attosecond electron dynamics involve the exchange of at least two photons, this is a general and significant effect that must be taken into account in all measurements of time delays involving photoionization processes.

I. INTRODUCTION

The advent of attosecond science [1,2] (1 as = 10^{-18} s) paved the way towards studying and understanding the nature of electron dynamics in atomic, molecular and condensed matter systems on their natural time scale [3-15]. In particular, recent experimental studies in atomic systems [3,6-9] confirmed the ability of attosecond science to unravel ultrafast electron dynamics with high accuracy. A series of

groundbreaking investigations [6,10-15] have established attosecond metrology as a new indispensable tool in atomic, molecular, and optical physics.

Extremely small time delays in electron emission induced by single-photon atomic absorption have been measured with two different techniques, attosecond streaking [3,16] and RABBITT (reconstruction of attosecond beating by interference of two-photon transitions) [1,7]. These methods are based on single-photon ionization, realized in a non-sequential pump-probe scheme, where the extreme ultraviolet (XUV) attosecond pump pulse ionizes the target system and an infrared (IR) probe pulse interacts with the liberated electrons. While attosecond streaking employs a single attosecond pulse (SAP), an attosecond pulse train (APT) is used in RABBITT. Neither technique gives access to absolute photoemission time delays. However, relative timing information between electrons originating from different states within the same atom [3,7] or from different atoms [9,17,18] can be extracted.

An alternative perspective on the photoemission process can be obtained by studying the relative timing of electrons emitted from the same initial state within the same target system but at different emission angles θ [19], relative to the polarization axis of the XUV and IR pulses (Fig. 1a).

With the attosecond streaking technique the emission of electrons is normally only recorded along the linear polarization axis of the IR field, for which the streaking of the photoelectron momentum features a pronounced single-sweep per laser period (ω-modulation). As the ejection-angle is changed from 0° to 90° relative to the linear polarization axis of the IR field, the streaking of the photoelectron momentum changes to a much weaker 2ω-modulation [16]. To avoid any mixing of electrons emitted at different angles, one must significantly decrease the IR streaking field

intensity, which makes the analysis of the experimental streaking traces more complex and demanding [20].

For the RABBITT technique, however, the directionality of the momentum transfer is of minor importance because the so-called sideband (SB) signals exhibit a 2ω-modulation for all ejection angles. Therefore, this method is better suited for exploring the angular dependence of photoemission time delays.

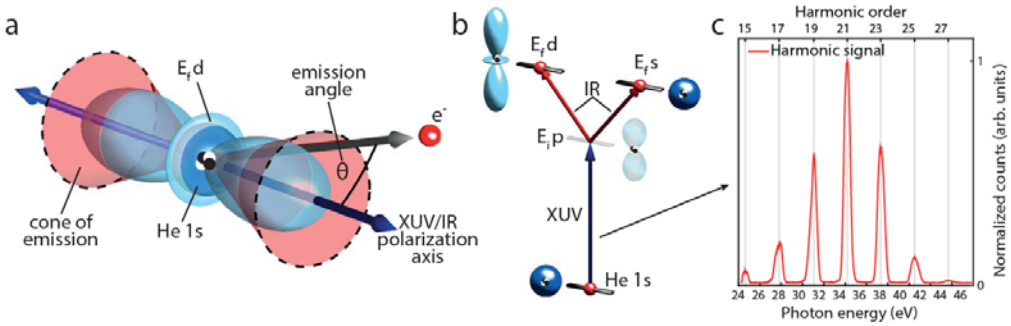

Figure 1 | Two-photon ionization pathways starting from ground state helium. a, Schematic defining the emission angle θ as the electron emission direction relative to the XUV and IR polarization axes and illustrating the different photoelectron partial waves of the corresponding final quantum states, which arise from the exchange of two photons. **b,** Schematic illustrating the different quantum paths, which contribute to the final state of the liberated photoelectrons after the interaction with the XUV and IR fields. **c,** XUV spectrum, which has been used to carry out the experiments.

In atomic photoionization, the absorption of a single photon causes electrons to be excited from their initial state $n_i\, l_i$ into the final state El. Here, $n(l)$ is the principal (orbital angular momentum) quantum number and E is the photoelectron energy. Since a photon itself carries a spin angular momentum of one unit (of $\hbar$), the allowed transitions $n_i\, l_i \rightarrow El$ with the absorption of a single photon result in a change in angular momentum of $\Delta l = \pm 1$ unit and therefore in two final quantum states with $l \rightarrow l \pm 1$. As shown in earlier work [21,22], the interplay between two different angular components may give rise to an anisotropic time delay τ_W (also known as Wigner time delay [23]) of the photoelectron wave packet, which is generated by the

absorption of one XUV photon. So far, the angular dependence of group delays was exclusively studied theoretically, and in the context of the ionization from a non-symmetric orbital [21,24]. Previous pioneering theoretical work on the angular dependence of photoionization, including the investigation of photoelectron angular distributions and associated anisotropies [25-27] was performed in the energy domain exclusively. In these studies, scattering phases were only determined at a single energy. Based on this work, first 'complete' photoionization measurements [28-30] provided access to the phases and amplitudes of the ionization matrix element. Here, we report on the angular dependence of the photoionization process in the time domain by probing the electron with a phase-locked laser field at several different photoelectron energies using RABBITT. This gives direct access to the relative angle-dependent scattering phase of the generated photoelectron wave packets. To our knowledge, this is the first experimental demonstration of this sort.

In the special case of starting from a spherically symmetric orbital *ns*, only a single photoionization transition $l \rightarrow l+1$ (i.e., $ns \rightarrow Ep$) is possible. If, in addition, the remaining ion is left in a spherically symmetric state, the orbital angular momentum of the photoelectron is conserved. In these conditions, the Wigner time delay is rigorously independent of the ejection angle. Therefore, the time delay measured with an attosecond interferometric technique was also expected to remain unaffected, provided that the further exchange of an IR photon did not induce additional angular modulations. Yet, as soon as two photons are involved in the ionization process, two different final states $1s \rightarrow E_i p \rightarrow E_f s/E_f d$ become accessible (Fig. 1b). As a result, the group delay of the final photoelectron wave packet may still exhibit an angular dependence. This would be the case, for example, if helium (He) was ionized from its spherically symmetric ground state. Indeed, while one expects an isotropic

photoemission time delay associated with the XUV absorption, a perturbative analysis (see appendix, section D) shows that the intrinsic two-photon nature of the interferometric measurement of the time delay introduces by itself an inherent, universal anisotropy in the measurement. To which extent such anisotropy affects measurements of photoemission time delays along fixed directions, is a fundamental question relevant for current attosecond spectroscopy. Partially because of the formidable challenge of angle-resolved measurements of photoemission time delays, this question has not been addressed by any experiment before.

Here, we present a rigorous experimental and theoretical investigation of the measurement-induced angle-dependent photoemission time delay of electrons removed from the spherically symmetric $^1S^e(1s^2)$ ground state of He to produce the spherically symmetric ion $He^+(1s)$. Full angular resolution is obtained with the recently developed "AttoCOLTRIMS" apparatus [31], which consists of a reaction microscope allowing for full 3D momentum detection [32], combined with an attosecond front-end providing XUV attosecond pulses. Using the RABBITT technique, we measure a significant angular dependence of the photoionization time delay, which can be as large as 60 attoseconds. We will show in the following that this effect arises naturally whenever the photoionization process involves the exchange of more than one photon and angular dependent time delay can reach few hundred attoseconds.

II. THE RABBITT PRINCIPLE

In RABBITT spectroscopy, an APT with photon energies in the XUV range (Fig. 1c) is used in combination with an IR probe pulse to trace the electron dynamics by recording the photoelectron kinetic energy as a function of the pump-probe delay τ.

In the frequency domain, an APT is formed by odd multiples of the fundamental frequency ω_{IR} of the driving IR laser pulses employed for high-harmonic generation. Therefore, photoelectrons extracted with an APT from the ground state of an atomic target, with ionization energy I_{p}, are promoted into the continuum at energies $E_{\mathrm{elec}} = E_{\mathrm{harm}} - I_{\mathrm{p}}$. Hence, E_{elec} mirrors the discrete harmonic energies $E_{\mathrm{harm}} = (2q+1)\cdot\hbar\omega_{\mathrm{IR}}$ of the exciting XUV spectrum, where q is an integer.

The subsequent interaction of the photoelectrons with the weak IR-probe field allows an additional absorption or emission of an IR photon, such that also energies corresponding to even multiples of the fundamental frequency become accessible. Thus, SBs appear in between two consecutive harmonics in the photoelectron spectrum. For each SB of order $2q$ there are two indistinguishable excitation pathways: (1) absorption of one photon from harmonic $2q$-1 followed by the *absorption* of an additional IR photon, and (2) absorption of one photon from harmonic $2q$+1 and subsequent *emission* of an IR photon. These two quantum paths interfere, leading to an oscillation of the SB amplitude A_{SB} when changing the delay τ between the APT and the IR pulses: $A_{\mathrm{SB}} \propto \cos(2\omega_{\mathrm{IR}}\tau - \Delta\phi_{\mathrm{atto}} - \Delta\phi_{\mathrm{atomic}})$. Here, $\Delta\phi_{\mathrm{atto}}$ is the phase difference between consecutive harmonics and corresponds to the group delay of the APT, $\tau_{\mathrm{atto}} \approx \Delta\phi_{\mathrm{atto}} / 2\omega_{\mathrm{IR}}$, while $\Delta\phi_{\mathrm{atomic}}$ corresponds to the so-called atomic time delay $\tau_{\mathrm{atomic}} \approx \Delta\phi_{\mathrm{atomic}} / 2\omega_{\mathrm{IR}}$.

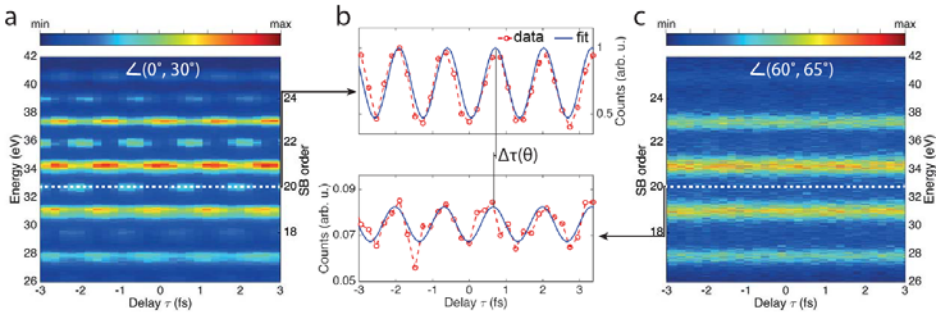

Figure 2 | Principle of the time delay extraction. a-c, Examples of measured RABBITT spectrograms and oscillations of sideband (SB) 20 (marked by white dashed lines) for different ranges in emission angle. Note that the energy scale corresponds to the sum of photoelectron kinetic energy and the ionization potential of helium (ionization potential of helium: 24.5874 eV [33]). In (**a**) only the photoelectrons detected within a 30° cone of emission (Fig. 1a) are selected. Panel (**c**) comprises photoelectrons emitted within a hollow cone of emission between 60° and 65°. Panel (**b**) shows an example of the intensity oscillations of SB 20 (red data points) obtained by integrating the counts within an energy window of 0.75 eV centered at the peaks of the SB oscillations (white dashed lines) together with their corresponding fits (blue solid lines). The time delay $\Delta\tau(\theta)$ is clearly visible as a temporal shift between the two different SB oscillations.

Theoretical models [34,35] established that the atomic delay τ_{atomic}, measured along the polarization direction can be divided into two contributions: the Wigner delay τ_{W}, originating from single-photon XUV ionization [36] and a measurement-induced component τ_{CC}. The measurement-induced component arises due to the additional quantum transition between two electronic states in the continuum induced by the IR-probe pulse.

To date, the possible dependence of τ_{CC} on the photoemission angle has not been considered, because all measurements on photoionization time delays have used either angle-integrating detection schemes, such as a magnetic bottle spectrometer [7], or directional detectors using e.g. time-of-flight spectrometers [3].

In our RABBITT experiments we have access to all electron emission angles relative to the common XUV/IR polarization axis within one single measurement and

thus under the same experimental conditions. Therefore, the contribution from τ_{atto}, which is the same for all photoelectrons within the same SB, cancels and we have direct access to the relative atomic delay differences $\Delta\tau_{atomic}$ between electrons emitted at different angles.

To reveal the fundamental angular dependence of τ_{CC}, we performed our investigation with He. Together with atomic hydrogen, He is the only system where τ_W is rigorously isotropic. However, while both targets are the only atomic systems fully accessible to theory, H is much more challenging for experiments. Therefore, this fundamental study can be used as a benchmark.

III. EXPERIMENTAL SETUP

The experimental setup has been presented elsewhere [31]. In brief, we use a Ti:sapphire laser system providing IR-pulses with a duration of 30 fs and pulse energies up to 750 μJ at a repetition rate of 10 kHz. These pulses are focused into an Ar filled gas target to generate an APT pump-pulse in the XUV range. An aluminum foil with a thickness of 300 nm is used as a filter unit to remove the fundamental IR radiation copropagating with the XUV light. The IR probe-pulse is delayed with respect to the APTs by means of a piezoelectric delay stage in a separate probe arm and subsequently recombined with the XUV pump-pulse on a holey mirror. The two beams propagate collinearly and are focused by a toroidal mirror into the target gas jet of a reaction microscope detector, where ions and electrons are separated and guided towards time and position sensitive detectors by uniform electric and magnetic fields. This allows the retrieval of the 3D momentum vector of each individual fragment over the full 4π solid angle. Moreover, the delay between the XUV-pump and the IR-probe is actively stabilized in order to minimize potential sources of systematic errors

and to ensure attosecond stability. This is realized by means of a feedback-loop, which stabilizes the phase of the interference pattern of two overlapping blue laser beams, which copropagate until the holey mirror along the same optics as compared to the XUV-pump and IR-probe pulses.

IV. **EXPERIMENTAL RESULTS**

Figure 2 shows the results of the present angle-resolved RABBITT measurements. Applying an angular filter on the detected photoelectrons, i.e. choosing electrons emitted within the corresponding cone of emission (Fig. 1a), we are able to obtain distinct RABBITT traces representing only photoelectrons out of particular hollow cones (Figs. 2a, 2c). For any angular sector, the SB signal is obtained by integrating the spectrogram in an energy window ΔE=0.75 eV centered at the peak of the SB position. Two curves showing the SB signal are presented in Fig. 2b for photoelectrons emitted between 0° and 30° (top panel) and between 60° and 65° (lower panel).

While the SB beating at small angles is clearly visible even in the energy resolved spectrum (Fig. 2a), it is barely discernible at large angles (Fig. 2c). When the SB signals are integrated in energy, however, the characteristic oscillations with periodicity $2\omega_{IR}$ appear for both angular ranges (Fig. 2b) and thus a clear angle-dependent delay $\Delta\tau(\theta)$ can be extracted. This is the delay between electrons emitted into a specific hollow cone between θ and $\theta+\Delta\theta$ (Fig. 1a) and electrons emitted at angles between 0° and 30° (reference). Note that the angular range of the reference

has been chosen to be as wide as 30º in order to improve its signal-to-noise ratio and thus to minimize the error in the retrieval of the relative phase.

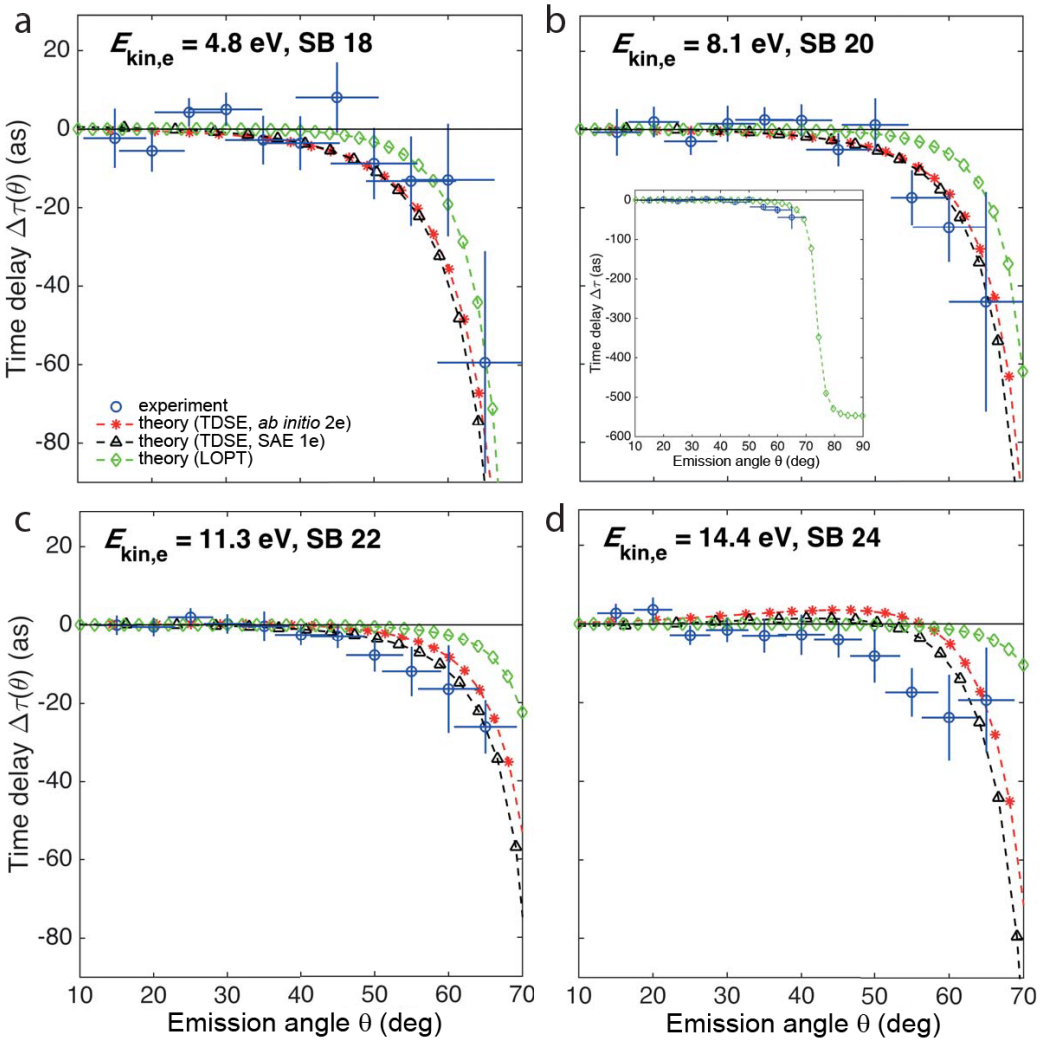

Figure 3 | Angular dependence of photoemission time delays in helium for different photoelectron kinetic energies. a-d, For all photoelectron kinetic energies, referenced by the sidebands (SBs) of the harmonic spectrum of the attosecond XUV pulse train, the experimentally retrieved atomic delay (blue data points with error bars) is shown as a function of the emission angle θ, following the procedure described in Fig. 2. For example, a delay at 15° is understood as the delay between photoelectrons emitted at angles between 10° and 15° and photoelectrons emitted between 0° and 30° (reference). As a comparison, the corresponding theoretical predictions are also included in the graphs comprising an *ab initio* simulation (red dashed line with asterisks), where the time-dependent Schrödinger equation (TDSE) is solved using a nearly exact method [37] taking into account both electrons in He, a calculation solving the TDSE within the single-active electron (SAE) approximation

(black dashed line with triangles) and lowest-order perturbation-theory (LOPT) calculation (green dashed line with diamonds). The different theories are in very good agreement and reproduce the experimental data well. The inset in (**b**) shows the typical behavior of the angle-dependent delay predicted by LOPT for an angular range up to 90°. As a consequence of the node in the *d*-wave, at large emission angles θ the delay changes significantly.

The measured angle-resolved photoemission time delays relative to the zero emission angles are shown with error bars in Fig. 3 for four consecutive SBs, SB 18-SB 24. For all SBs the measurements deviate significantly from zero for angles larger than 50°. The largest anisotropy is recorded for the lowest sideband, but it is statistically significant in all cases. As can be seen in Fig. 2b, the accuracy of the fit decreases at larger emission angles due to the smaller count rate of the SB signals. This explains the larger error bars at larger emission angles in Fig. 3.

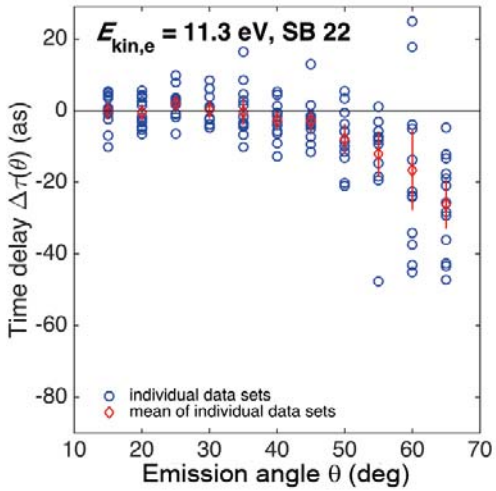

Figure 4 | Spread of the data extracted from individual data sets and error estimation for SB 22. Spread of 13 individual data sets (blue circles) for each of the considered angular sectors. The means of the 13 individual data sets for each angular sector are shown as red diamonds. The according error bars correspond to the standard deviation of the 13 individual data sets at each angular sector.

Fig. 4 shows for the example of SB 22 how the error bars in $\Delta\tau(\theta)$ and θ are estimated. The data shown in Fig. 3 correspond to the mean value of 13 individual

data sets for each angular sector θ. The error $\Delta\big(\Delta\tau(\theta)\big)$ at each of the considered emission angles θ was determined by calculating the standard deviation of the delays extracted from the 13 individual data sets:

$$\Delta\big(\Delta\tau(\theta)\big) = \sqrt{\frac{1}{N-1}\sum_{i=1}^{N}\big(\overline{\Delta\tau}(\theta) - \Delta\tau_i(\theta)\big)^2} \ .$$

Here, $N = 13$ indicates the number of individual measurements and $\overline{\Delta\tau}(\theta)$ corresponds to the mean value of all individual measurements at a certain emission angle θ. Moreover, $\Delta\tau_i(\theta)$ represents the values of a single time delay measurement i at a distinct emission angle θ.

The error in θ is dominated by the finite momentum resolution of the electron detector. Since the photoelectron momentum component parallel to the XUV-IR polarization direction exhibits the best resolution, the error of θ increases with larger emission angles. Moreover, the error in θ decreases with larger photoelectron energies.

Since the time-of-flight (TOF) axis of the detector used for electron detection served as a reference direction, special care was taken that the polarization axis of the XUV pulses was aligned parallel to the TOF axis. To achieve parallel alignment, the XUV polarization axis was adjusted until the photoelectron spectra yielded a symmetric pattern in the XUV polarization plane relative to the TOF axis.

III. THEORY AND DISCUSSION

To validate and explain the experimental observations, we used different theoretical models. First, we performed *ab initio* simulations, solving the full dimensional time-dependent Schrödinger equation (TDSE) by using a nearly exact

method [37], which takes into account both electrons in He, as well as the parameters of the linearly polarized pulses used in the experiment.

In the time-dependent *ab initio* method, the wave function is expanded on a two-particle spherical basis, where the angular part is represented with bipolar spherical harmonics and the radial parts with B-spline functions [38]. For each total angular momentum L= 0, 1, …, 10, the configuration space comprises a close-coupling sector, given by a selection of relevant partial-wave ionization channels where an He^+ parent ion Nl is angularly and spin coupled to a second electron in a generalized orbital εl', and a localized sector, given by all the configurations $nln'l'$ formed from localized orbitals appropriate to represent the short-range (dynamical) correlations between the two electrons not accounted for by the close-coupling configurations [39]. In the partial wave channels Nl εl', the parent ions are restricted to N≤2, the orbital angular momentum for the second electron is limited to l'≤11, and the radial part is spanned by the B-splines of order 8, defined on a grid with asymptotic uniform spacing of 0.5 a.u., up to a maximum radius of 1200 a.u. Such a quantization box permits the full representation of the ionization wave packet in the conditions of the RABBITT experiment examined in this paper for a duration up to 35 fs. The localized channels include all the configurations $nln'l'$, with l,l'<5, obtained from a set of B-splines restricted to a limited radial range of approximately 40 Bohr radii. The initial bound state of the atom is obtained by fully diagonalizing the Hamiltonian in the $^1S^e$ sector of the basis. The same basis is used to compute the scattering states of the atom, i.e., the continuum states above the ionization threshold that fulfill prescribed boundary conditions, by solving the Lippmann-Schwinger equation with the K-matrix method [39]. Starting from the $1s^2$ ground state, we integrate the time-dependent Schrödinger equation for the atom under the influence of

the external pulses using a second-order unitary split-exponential time-step propagator in either velocity or length gauge [40].

An exponential propagator that includes the Coulomb and/or the kinetic part of the field-free Hamiltonian H_0 may exhibit stiffness issues, unless special precautions are taken. In our case, we follow a procedure that completely eliminates any potential stability or convergence issue associated to the Coulomb divergence or to the large span of the kinetic operator spectrum. Namely, we carry out the time propagation in the basis of Eigenstates of the field-free Hamiltonian. In such a basis, the most natural choice for a second-order exponential propagator is

$$U(t+dt,t) = \exp\left(-iH_0\frac{dt}{2}\right)\cdot\exp[-i\alpha A_z(t)P_z]\cdot\exp\left(-iH_0\frac{dt}{2}\right),$$

since, within this splitting scheme, the action of the first and last steps can be evaluated exactly, and it includes the effects of both the Coulomb and the kinetic terms. Only the intermediate exponential is estimated numerically, using the Krylov method, an iterative procedure that preserves unitarity. This step does not pose any stability or convergence problem, owing both to the good behavior of the canonical momentum operator and to the weakness of the external field employed for the current simulations. From a numerical perspective, this approach amounts to cure the potential stiffness issues of the TDSE propagator with the best time-independent preconditioner possible.

At the end of the propagation, as soon as the external pulse is over, the fully differential distribution of the photoelectron is extracted from the wave packet by projecting it on the scattering states of the atom [37,40,41]. Our results are found not to depend on the gauge.

This method reproduces accurately the atomic dynamics taking into account the real pulses used in the actual experiments. To all practical purposes, the TDSE *ab initio* results are expected to be a faithful numerical replica of the real experiment.

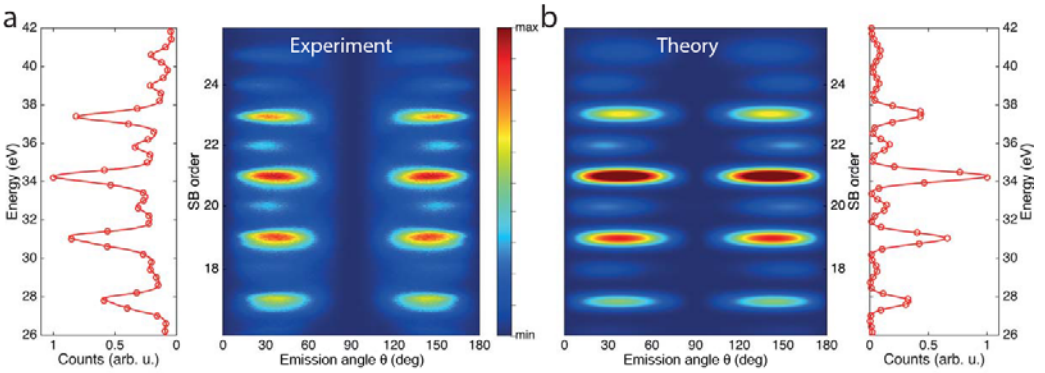

Figure 5 | Comparison between experiment and TDSE *ab initio* (2 electrons) simulation. a, Experimental data. **b,** Results of the TDSE *ab initio* (2 electrons) calculation. The 2D plots show the delay-integrated photoelectron spectrum as a function of the emission angle θ, defined in Fig. 1a. On the left and right hand side of (**a**) and (**b**), respectively, the angle-integrated projections for experiment and theory highlight the presence of four SBs comprising SB 18 to SB 24.

Figure 5 shows a comparison between the time delay integrated photoelectron spectra measured in the experiment for a moderately weak ($3\text{x}10^{11}$ W/cm^2) IR probe pulse with a center wavelength of 780 nm and the spectrum computed *ab initio* using pulse parameters that match the experimental ones. Figure 3 shows the comparison of the time delays $\Delta\tau$ for the energy integrated SB signals. The results of the TDSE *ab initio* calculations are in quantitative agreement with the measurement. For SB 18 the experimental data slightly deviate from the theoretical estimates as compared to the other SBs. We attribute these deviations to the low intensity of SB 18 and consequently to a noisier signal, reflected also in larger error bars. Nevertheless, for the considered angular range, the discrepancy between experimental data and the theory curves is not larger than 10-15 as, which we consider fairly acceptable given the complexity of experiment and theory.

It is known, that the finite duration of the pulses gives rise to harmonics with a finite width, whose tail partly overlaps with the sidebands in the energy-resolved photoelectron spectrum. This effect, which is entirely negligible for angle-integrated measurements, is noticeable in angle-resolved measurements.

Figure 6 studies the effect of this contamination on the SB signal for the example of SB 18 in helium. As the energy integration interval ΔE across the peak position of the SB signal increases, the anisotropy becomes larger. This observation is attributed to the increasing contribution of the neighboring HH signals to the considered SB signal.

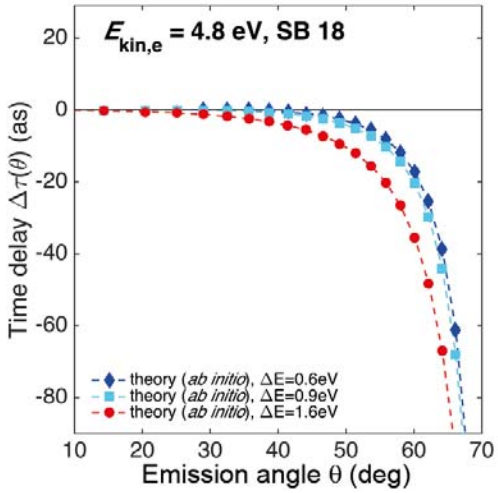

Figure 6 | Effect of contamination in *ab initio* calculations on SB 18 in helium. Results of the angular anisotropy obtained from *ab initio* calculations using three distinct integration intervals ΔE. For the results represented by the red dashed line with circles ΔE=1.6 eV was considered, while the calculations yielding the blue and cyan dashed lines with stars considered ΔE=0.9 eV and ΔE=0.6 eV, respectively.

As shown in Fig. 5, the SB signals obtained from the experimental data are significantly more contaminated by the neighboring HH signals (Fig. 5a) as compared to the SB signals extracted from the theoretical calculations (Fig. 5b). For this reason, the energy integration window used for the *ab initio* theory was chosen to be larger in

order to take this contamination effect into account. For the calculations shown in Fig. 3 an energy integration interval of ΔE=1.6 eV was chosen. This value properly reproduces the contamination present in the experimental data.

To ensure that the observed anisotropy is still present in absence of any spectral overlap from the harmonics, we repeated the TDSE *ab initio* simulations with long and linearly polarized XUV pulses. The results of these calculations were compared with the predictions of time-independent lowest-order perturbation-theory (LOPT) calculations that assume infinitely long and linearly polarized pulses.

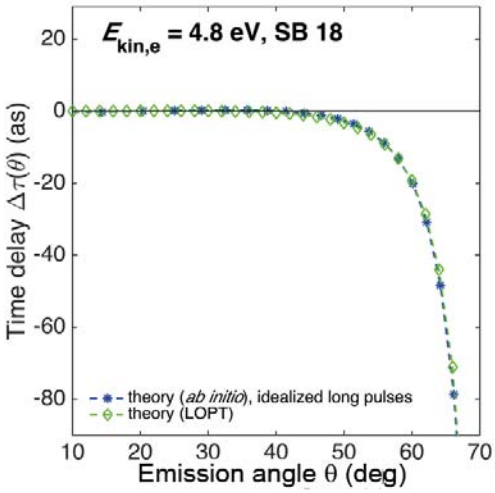

Figure 7 | Comparison between TDSE *ab initio* 2 electrons and LOPT calculations in helium for SB 18 using idealized long pulses. The results obtained from TDSE *ab initio* 2 electrons (blue dashed line with asterisks) and LOPT (green dashed line with diamonds) calculations are in excellent agreement. This confirms that the discrepancy between the LOPT and the time-dependent simulations in Fig. 3 may be attributed to the effect of contamination.

Since the two calculations are in excellent agreement (see Fig. 7), in Fig. 3 we only present the results of the LOPT calculations (dashed green line with diamonds). Even if the time-delay anisotropy of this second set of calculations is smaller than before, the effect is still clearly visible, and in particular, the sharp drop around 50° is reproduced.

The atomic delay LOPT calculations are performed using correlated two-photon (XUV+IR) matrix elements on an exterior complex scaled basis set [21] and account for ground-state correlation effects during single-photon absorption.

Many-body effects are included to the level of the Random Phase Approximation with Exchange (RPAE) for the XUV photon, while the final state is approximated as an ingoing scattering state in a spherical effective potential corresponding to the K=0 projected-hole potential of the 1*s* orbital. The Hartree-Fock ionization potential of helium, $I_{1s}^{(HF)}$=25.0 eV, is substituted by the experimental value, $I_{1s}^{(EXP)}$=24.6 eV. The delay at SB 18 is computed using a B-spline grid with exterior complex scaling (ECS) starting at 75 Bohr radii; while a more modest grid, with ECS at 35 Bohr radii, is sufficient for the delay at SB 20-24. The grid spacing in the intermediate regime as 0.5 Bohr radius, while some additional grid points are added close to the core. More details about the two-photon matrix element method and the angle-resolved atomic delay in argon is found elsewhere [21].

Additional LOPT calculations are performed where the ground-state correlation between the two active electrons in He is omitted. The omission of this effect is found to have virtually no effect on the delay, which implies that the anisotropy is not sensitive to ground-state correlation effects. However, the interaction with the additional field is treated as an uncorrelated transition. Hence, if final-state correlation effects become significant, LOPT may fail in explaining the observed experimental results.

In contrast to ground-state correlation effects, we have found that including the reversed time ordering of the photon absorption (IR+XUV) leads to a correction that is approximately 10% at from 50 to 70 degrees, see Fig. 8.

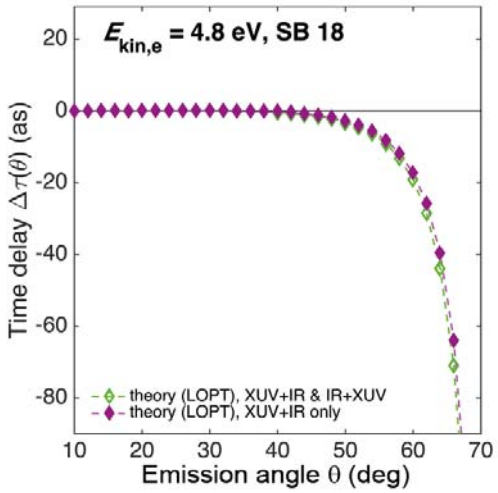

Figure 8 | Comparison between distinct LOPT calculations in helium for SB 18. The results of lowest-order perturbation theory (LOPT) calculations considering a single two-photon process (XUV+IR) and additionally its reversed time-ordering (XUV+IR and IR+XUV) are shown as dashed lines with violet filled and green open diamonds, respectively.

Effects of this kind, as well as field convolution effects, are automatically included by solving the problem in the time domain. Hence, the discrepancy between the LOPT results and the time-dependent simulations in Fig. 3 may be safely attributed to above mentioned contamination effect.

Within LOPT, the anisotropy of the time delay can be explained with an analytical description, which gives better physical insight into this anisotropy. As described in the introduction, if two linearly polarized photons are involved in the ionization of He, two different final states become accessible, represented by an *s*- or a *d*-wave. The angular shape of each final state can be described by distinct spherical harmonics, Y_l^m, with l (m) representing the orbital angular momentum (magnetic) quantum number. While the Y_0^0 spherical harmonic, representing the *s*-wave, is isotropic, the Y_2^0 spherical harmonic associated with the *d*-wave exhibits a node at the magic angle of 54.7°. Therefore, the interference between the transitions in the continuum mediated by the IR pulse is expected to lead to an angular dependence of

the atomic time delay. The variation of the delay is expected to become particularly pronounced when the emission direction of the photoelectrons with respect to the common XUV/IR polarization axis approaches 60°. We can parametrize the observed angle-dependent delay in the special case of He as follows:

$$\Delta\tau(\theta) \propto \arg\left({1 + T^{-}(\theta)} \Big/ {1 + T^{+}(\theta)} \right), \quad (1)$$

with $T^{\pm}(\theta) = \sqrt{4\pi} \cdot c_{\pm}^{ds} \cdot e^{i\phi_{\pm}^{ds}} \cdot Y_2^0(\theta, 0)$. Here, $c_{\pm}^{ds} = \left| A_{\pm}^{d} / A_{\pm}^{s} \right|$ and $\phi_{\pm}^{ds} = \arg\left(A_{\pm}^{d} / A_{\pm}^{s} \right)$ are the absolute values and phases of the two-photon transition amplitudes representing the four quantum paths *s* → *p* → *s* (+/-) and *s* → *p* → *d* (+/-). The symbol (+) indicates the transition involving the absorption of an IR photon and (-) represents the transition, which involves the emission of an IR photon.

The inset in Fig. 3b shows the behavior of the angle-dependent delay predicted by LOPT up to 90°. As soon as the magic angle of approximately θ=54.7° is reached, the *d*-wave changes sign and therefore exhibits a significant change in delay, which can be as large as 600 attoseconds for values of θ above 80 degrees (see inset in Fig. 3b), i.e. well outside the experimentally accessible angular range. This strong variation can be attributed to the phase jump by one unit of π which corresponds to $\tau = {\pi}/{2\omega} = 667$ as.

A fit of the theoretical curves presented in Fig. 3 allows for the extraction of the moduli and phases of the transition amplitudes for each model. The result of this procedure is presented in Table 1. As a consequence of the agreement between the different theories in Fig. 3, the corresponding extracted values are consistent with each other.

The lack of experimental data for large angles in case of the He target prevents us from performing the same analysis on the experimental data. However, we note that the strongest angular dependence of the time delay occurs well above the magic angle. This effect can be interpreted as an indication of approximately equal strength of the *s*- and *d*-continua in contrast to what was observed in Ref. [21,22].

		c_-^{ds}	c_+^{ds}	ϕ_-^{ds}	ϕ_+^{ds}
SB18	TDSE *ab initio* (2e)	1.233±0.001	0.518±0.012	0.217±0.001	0.155±0.006
	TDSE SAE (1e)	1.276±0.001	0.536±0.011	0.232±0.001	0.160±0.006
	LOPT	1.331±0.001	0.563±0.006	0.166±0.001	0.157±0.003
SB20	TDSE *ab initio* (2e)	1.134±0.001	0.497±0.025	0.122±0.001	0.107±0.009
	TDSE SAE (1e)	1.168±0.001	0.603±0.008	0.128±0.001	0.090±0.003
	LOPT	1.171±0.001	0.623±0.015	0.066±0.004	0.061±0.003
SB22	TDSE *ab initio* (2e)	1.075±0.001	0.361±0.057	0.087±0.001	0.121±0.023
	TDSE SAE (1e)	1.105±0.002	0.266±0.116	0.096±0.002	0.138±0.063
	LOPT	1.094±0.001	0.674±0.006	0.034±0.001	0.030±0.002
SB24	TDSE *ab initio* (2e)	1.083±0.001	0.477±0.002	0.137±0.001	0.198±0.002
	TDSE SAE (1e)	1.134±0.001	0.488±0.005	0.145±0.001	0.188±0.002
	LOPT	1.046±0.020	-0.010±0.3	0.021±0.001	-1.501±0.32

Table 1 | Parameters of the two-photon transition amplitudes. For each SB, the analytical formula (Eq. 1) is used to fit the angular anisotropy predicted by each model. The absolute values and phases of the two-photon transition amplitudes can be extracted as fitting parameters.

Other targets may have a smaller critical angle, which then would be more easily accessible with our experimental setup. In that case a robust parameterization of the time delay angular dependence could be obtained, thus providing a simple analytical way to estimate the degree of anisotropy in such kind of measurements.

In contrast to the other SBs, theory predicts a slightly positive delay for SB 24 at angles smaller than about 55°, a trend that is not observed in the experimental data (Fig. 3). We attribute this effect to the spectral overlap of SB 24 with its two neighboring harmonics 23 and 25 for which the difference in intensity is the largest (Fig. 1c).

The question remains, whether the angular modulation in the relative phase between the *s*- and the *d*-waves may be affected by the correlation between the two active electrons in He. To answer this question, we have solved the TDSE using a single-active electron (SAE) model with the field-free He atom described by an effective one-electron potential [42]. Full details of these simulations are presented elsewhere [43]. In brief, the solution of the TDSE is presented as a partial wave series with the number of partial waves limited to $L_{max} = 4$. This ensures convergence in the velocity gauge of the electromagnetic interaction. The radial part of the TDSE is discretized on the grid with the stepsize $\delta r = 0.05$ a.u. in a box of the size Rmax = 400 a.u. Substitution of the partial wave expansion into the TDSE gives a system of coupled equations for the radial functions, describing evolution of the system in time. To solve this system, we use the matrix iteration method [44]. The ionization amplitudes a($\boldsymbol{k}$) are obtained by projecting the solution of the TDSE at the end of the laser pulse on the set of the ingoing scattering states of the target atom. Squaring of the amplitudes a($\boldsymbol{k}$) gives the photoelectron spectrum in a given direction determined by the azimuthal angle θ. After collecting the photoelectron spectra in various directions, the SB intensity oscillation with the variable time delay between the APT and IR fields is fitted with the cosine function described before, $\mathrm{SB} \propto \cos\left(2\omega_{\mathrm{IR}}\tau - \Delta\phi_{\mathrm{atto}} - \Delta\phi_{\mathrm{atomic}}\right)$, using the non-linear Marquardt-Levenberg

algorithm. The quality of the fit is very good with the errors in fitting parameters not exceeding 1%.

In the TDSE SAE calculations, we used the parameters of the linearly polarized pulses employed in the experiment and followed a strategy tested in previous studies [45]. This model is known to reproduce well both the ionization potential of He and its single-photon ionization cross section. However, by construction, it does not account for any exchange or correlation effects between the two active electrons in He. The predictions of this model are shown for all SBs in Fig. 3 as black dashed lines with triangles. These results are similar to the values obtained from *ab initio* calculations (red dashed lines with asterisks).

IV. CONCLUSIONS AND OUTLOOK

We have provided the first experimental evidence of an angular dependence in the measurement of photoemission time delays. These measurements are based on single-photon ionization, realized in a non-sequential pump-probe scheme where the extreme ultraviolet (XUV) attosecond pump pulse ionizes the target system and an infrared (IR) probe pulse interacts with the liberated electrons. We have observed an angular dependence even when the single-photon emission delay is rigorously isotropic. This photoemission angular dependence results from the interference between two different final quantum states accessible in two-photon processes. The measured delays are in excellent agreement with those obtained from fully TDSE *ab initio* calculations.

The above conclusions apply to most attosecond measurement techniques, such as streaking and RABBITT. This knowledge may shed new light on previous experiments performed in gaseous [3,7] and condensed matter systems [5], where the

angular dependence of the measured time delays was not always taken into account and where in most cases SAE approximations have been used.

ACKNOWLEDGEMENTS

S.H, C.C, L.G. and U.K. acknowledge support by the ERC advanced grant ERC-2012-ADG_20120216 within the seventh framework program of the European Union and by the NCCR MUST, funded by the Swiss National Science Foundation. M.L. acknowledges support from the ETH Zurich Postdoctoral Fellowship Program.

Á.J.G., L.A. and F.M. acknowledge the support from the European Research Council under the ERC grant no. 290853 XCHEM, from the European COST Action CM1204 XLIC, the MINECO Project FIS2013-42002-R, the ERA-Chemistry Project PIM2010EEC- 00751, and the European Grant MC-ITN CORINF. Calculations were performed at the Centro de Computación Científica of the Universidad Autónoma de Madrid (CC-UAM) and the Barcelona Supercomputing Center (BSC).

I.I. and A.S.K. acknowledge support of the Australian Research Council (DP120101805) and the use of the National Computational Infrastructure Facility.

J. M. D acknowledges support from the Swedish Research Grant No. 2013-344 and 2014-3724. E. L. acknowledges support from the Swedish Research Council, Grant No. 2012-3668.

Moreover, this research was supported in part by the Kavli Institute for Theoretical Physics (National Science Foundation under Grant No. NSF PHY11-25915) and by NORDITA, the Nordic Institute for Theoretical Physics.

References

[1] P. M. Paul, E. S. Toma, P. Breger, G. Mullot, F. Augé, P. Balcou, H. G. Muller, and P. Agostini, Science **292**, 1689 (2001).
[2] M. Hentschel *et al.*, Nature **414**, 509 (2001).
[3] M. Schultze *et al.*, Science **328**, 1658 (2010).
[4] G. Sansone *et al.*, Nature **465**, 763 (2010).
[5] A. L. Cavalieri *et al.*, Nature **449**, 1029 (2007).
[6] P. Eckle, A. N. Pfeiffer, C. Cirelli, A. Staudte, R. Dörner, H. G. Muller, M. Büttiker, and U. Keller, Science **322**, 1525 (2008).
[7] K. Klünder *et al.*, Physical Review Letters **106**, 143002 (2011).
[8] C. Ott *et al.*, Nature **516**, 374 (2014).
[9] M. Sabbar, S. Heuser, R. Boge, M. Lucchini, T. Carette, E. Lindroth, L. Gallmann, C. Cirelli, and U. Keller, Physical review letters **115**, 133001 (2015).
[10] M. Schultze *et al.*, Nature **493**, 75 (2013).
[11] H. J. Wörner, J. B. Bertrand, D. V. Kartashov, P. B. Corkum, and D. M. Villeneuve, Nature **466**, 604 (2010).
[12] F. Calegari *et al.*, Science **336**, 336 (2014).
[13] A. S. Landsman, M. Weger, J. Maurer, R. Boge, A. Ludwig, S. Heuser, C. Cirelli, L. Gallmann, and U. Keller, Optica **1**, 343 (2014).
[14] R. Locher, L. Castiglioni, M. Lucchini, M. Greif, L. Gallmann, J. Osterwalder, M. Hengsberger, and U. Keller, Optica **2**, 405 (2015).
[15] E. Goulielmakis *et al.*, Nature **466**, 739 (2010).
[16] J. Itatani, F. Quéré, G. L. Yudin, M. Y. Ivanov, F. Krausz, and P. B. Corkum, Physical Review Letters **88**, 173903 (2002).
[17] C. Palatchi, J. M. Dahlström, A. S. Kheifets, I. A. Ivanov, D. M. Canaday, P. Agostini, and L. F. DiMauro, Journal of Physics B: Atomic, Molecular and Optical Physics **47**, 245003 (2014).
[18] D. Guénot *et al.*, J. Phys. B **47**, 245602 (2014).
[19] O. Guyétand *et al.*, J. Phys. B: At. Mol. Opt. Phys. **41**, 051002 (2008).
[20] K. Zhao, Q. Zhang, M. Chini, Y. Wu, X. Wang, and Z. Chang, Optics Letters **37**, 3891 (2012).
[21] J. M. Dahlström and E. Lindroth, Journal of Physics B: Atomic, Molecular and Optical Physics **47**, 124012 (2014).
[22] J. Wätzel, A. S. Moskalenko, Y. Pavlyukh, and J. Berakdar, Journal of Physics B: Atomic, Molecular and Optical Physics **48**, 025602 (2014).
[23] E. P. Wigner, Physical Review **98**, 145 (1955).
[24] J. M. Dahlström, D. Guénot, K. Klünder, M. Gisselbrecht, J. Mauritsson, A. L'Huillier, A. Maquet, and R. Taïeb, Chem. Phys. **414**, 53 (2013).
[25] J. Cooper and R. Zare, The Journal of Chemical Physics **48**, 942 (1968).
[26] J. L. Dehmer and D. Dill, Physical Review Letters **37**, 1049 (1976).
[27] S. N. Dixit and L. P., Physical Review A **27**, 861 (1983).
[28] P. Hockett, M. Wollenhaupt, C. Lux, and T. Baumert, Physical review letters **112**, 223001 (2014).
[29] K. Reid, D. Leahy, and R. Zare, The Journal of chemical physics **95**, 1746 (1991).
[30] Y. Y. Yin, C. Chen, D. S. Elliott, and A. V. Smith, Physical review letters **69**, 2353 (1992).

[31] M. Sabbar, S. Heuser, R. Boge, M. Lucchini, L. Gallmann, C. Cirelli, and U. Keller, Review of Scientific Instruments **85**, 103113 (2014).
[32] R. Dörner, V. Mergel, O. Jagutzki, L. Spielberger, J. Ullrich, R. Moshammer, and H. Schmidt-Bocking, Physics Reports **330**, 95 (2000).
[33] D. Z. Kandula, C. Gohle, T. J. Pinkert, W. Ubachs, and K. S. E. Eikema, Phys. Rev. Lett. **105**, 063001 (2010).
[34] S. Nagele, R. Pazourek, J. Feist, K. Doblhoff-Dier, C. Lemell, K. Tökési, and J. Burgdörfer, Journal of Physics B: Atomic, Molecular and Optical Physics **44**, 081001 (2011).
[35] J. M. Dahlström, T. Carette, and E. Lindroth, Physical Review A **86**, 061402 (2012).
[36] A. S. Kheifets and I. A. Ivanov, Physical Review Letters **105**, 233002 (2010).
[37] A. Jiménez-Galán, L. Argenti, and F. Martin, Physical Review Letters **113**, 263001 (2014).
[38] H. Bachau, E. Cormier, P. Decleva, J. E. Hansen, and F. Martín, Reports on Progress in Physics **64**, 1815 (2001).
[39] L. Argenti and R. Moccia, Journal of Physics B: Atomic, Molecular and Optical Physics **39**, 2773 (2006).
[40] L. Argenti and E. Lindroth, Physical Review Letters **105**, 053002 (2010).
[41] L. Argenti, R. Pazourek, J. Feist, S. Nagele, M. Liertzer, E. Persson, J. Burgdörfer, and E. Lindroth, Physical Review A **87**, 053405 (2013).
[42] A. Sarsa, F. J. Gálvez, and E. Buendía, Atomic Data and Nuclear Data Tables **88**, 163 (2004).
[43] I. A. Ivanov, J. M. Dahlström, E. Lindroth, and A. S. Kheifets, arxiv:1605.04539 (2016), Journal of Physics B, submitted.
[44] M. Nurhuda and F. H. Faisal, Physical Review A **60**, 3125 (1999).
[45] I. A. Ivanov and A. S. Kheifets, Physical Review A **8**, 033407 (2013).